AGU PUBLICATIONS

Geochemistry, Geophysics, Geosystems

RESEARCH ARTICLE

10.1002/2014GC005681

Key Points:
- Instability of cratonic lithosphere with non-Newtonian rheology is studied
- The instability is episodic and prolonged and starts at shallow depths
- The instability explains observations of destabilized North China Craton

Correspondence to:
S. Zhong,
szhong@colorado.edu
J. Huang,
jshhuang@ustc.edu.cn

Citation:
Wang, Y., J. Huang, and S. Zhong (2015), Episodic and multistaged gravitational instability of cratonic lithosphere and its implications for reactivation of the North China Craton, *Geochem. Geophys. Geosyst.*, *16*, 815–833, doi:10.1002/2014GC005681.

Received 5 DEC 2014
Accepted 9 FEB 2015
Accepted article online 19 FEB 2015
Published online 24 MAR 2015

Episodic and multistaged gravitational instability of cratonic lithosphere and its implications for reactivation of the North China Craton

Yongming Wang[1], Jinshui Huang[1], and Shijie Zhong[2]

[1]School of Earth Space Sciences, University of Science and Technology of China, Hefei, China, [2]Department of Physics, University of Colorado at Boulder, Boulder, Colorado, USA

Abstract Archean cratons are the most stable tectonic units and their lithospheric mantle is chemically depleted and buoyant relative to the underlying mantle. The chemical depletion leads to high viscosity that maintains the long-term stability of cratons. However, the eastern part of the North China Craton (~1200 km in horizontal length scale) had been extensively reactivated and modified over a time scale of ~100 Myr in the Mesozoic and Cenozoic. While the causes for the weakening of the North China Craton, a necessary condition for its reactivation, are still in debate, we investigate gravitational instability of compositionally buoyant lithosphere, by computing 2-D thermochemical convection models with different buoyancy number, lithospheric viscosity, and rheology. We find that the gravitational instability of cratonic lithosphere can happen over a larger range of buoyancy numbers with non-Newtonian rheology, but lithospheric instability with Newtonian rheology only happens with relatively small buoyancy numbers. For cratonic lithosphere with non-Newtonian rheology and relatively weak temperature-dependent viscosity, the instability starts in the cold, shallow part of the lithosphere and has small horizontal length scale (<300 km), leading to efficient thermal and chemical mixing with the underlying mantle. For cratonic lithosphere such as the eastern North China Craton, the instability process is episodic and consists of multiple instability events that may last for ~100 Myr. The instability process revealed from our study explains the observations of episodic magmatism/volcanism events, geochemical mixing, and time scales associated with the reactivation of the North China Craton.

1. Introduction

Archean cratons represent the oldest (>3 Ga) and thickest (~250 km) stable tectonic units on the Earth and are characterized by low surface heat flux and mantle lithosphere with fast seismic speeds, low temperature, and melt-depleted compositions [e.g., *Carlson et al.*, 2005; *Foley*, 2008; *King*, 2005; *Lee et al.*, 2011]. The melt depletion leads to high viscosity and reduced intrinsic density for cratonic lithosphere [*Carlson et al.*, 2005], while its low temperature further increases viscosity which is the key to its long-term stability [*Lenardic and Moresi*, 1999; *Shapiro et al.*, 1999; *Sleep*, 2003]. However, not all the cratons are stable, and the North China Craton (NCC), for example, had undergone extensive modification and reactivation in the Mesozoic and Cenozoic as indicated by large-scale deformation, magmatic activities, and basin formation [*Menzies et al.*, 2007]. Therefore, the NCC provides a unique opportunity to study the (in)stability of cratonic lithosphere.

Geochemical studies of Paleozoic kimberlites showed that the NCC had a thick (~200 km) lithosphere of Archean age as recently as in the Ordovician [*Gao et al.*, 2002], but may have lost a large portion of its root during the Mesozoic and Cenozoic periods [*Griffin et al.*, 1998; *Menzies et al.*, 2007; *Xu*, 2001; *Zhang et al.*, 2003]. This has been corroborated by geophysical observations of relatively high surface heat flow (~65 mW/m^2) and thin lithosphere (~80 km) at the present [*Chen et al.*, 2009; *Menzies et al.*, 2007; *Zhu et al.*, 2012a]. The reactivation of the NCC may have been initiated in the Jurassic at ~190 Ma with emplacement of plutonic rocks and lasted for ~100 Myr until the late Cretaceous as documented in Nd isotopes [*Menzies et al.*, 2007; *Xu*, 2001]. Episodic magmatism/volcanism occurred in the late Jurassic at ~160 Ma [*Gao et al.*, 2004] and peaked in the Cretaceous around 110–130 Ma [*Wu et al.*, 2005; *Zhang et al.*, 2003]. Extensional basins were also formed during this period on the craton [*Menzies et al.*, 2007; *Zhu et al.*, 2012a]. It is suggested that by the Cenozoic the thick and cold cratonic lithosphere of the NCC may have been replaced with thin and hot oceanic-type lithosphere [*Menzies et al.*, 2007; *Xu*, 2001].

© 2015. American Geophysical Union. All Rights Reserved.

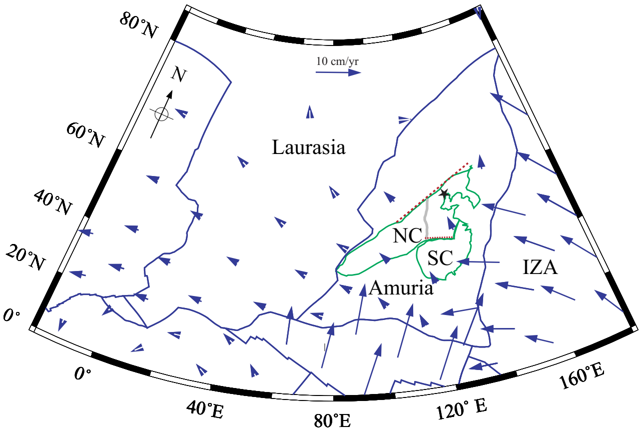

Figure 1. Tectonic map of the North China Craton and their surrounding blocks at 160 Ma ago from the GPlates [*Seton et al.*, 2012]. NC, SC, and IZA denote the North China block, South China block, and the Izanagi Plate. The gray line divides the NNC into the eastern and western parts. The red-dashed lines denote the suture zones between the North China and Siberia blocks, and the North China and South China blocks, respectively. The blue arrows represent plate motion.

However, the mechanism responsible for large-scale reactivation of Archean cratons including the NCC is still poorly understood. There have been two main proposals for the reactivation of the NCC. The first proposal emphasizes possible roles of subduction in reactivation of the NCC [e.g., *Zhu et al.*, 2012a]. The NCC as an overriding plate was adjacent to three subduction zones in the Paleozoic and Mesozoic (Figure 1): (1) to the south the subduction of the South China block until its collision with the NCC at 245–210 Ma [*Ames et al.*, 1993; *Li et al.*, 1993], (2) to the north, the subduction of the Siberia block and its merging with the NCC at ~250 Ma [*Kusky et al.*, 2007; *Xiao et al.*, 2003], and (3) to the east, the subduction of the Izanagi plate [*Seton et al.*, 2012]. Subduction may deliver water to the overriding plate (i.e., the NCC) to weaken the lithosphere, which is a necessary condition for destabilizing cratonic lithosphere [*Lee et al.*, 2011; *Lenardic et al.*, 2003; *Shapiro et al.*, 1999; *Sleep*, 2003], irrespective of physical mechanisms. Subduction of the Izanagi plate may cause extensional stress on the NCC, leading to thinning and reactivation of the NCC [*Zhu et al.*, 2012a, 2012b]. However, this model is largely a kinematic description with physical processes yet to be illustrated.

Second, gravitational instability of lithosphere (sometimes referred to as lithospheric delamination) was proposed to explain the high intensity of volcanism/magmatism and extensional events in the Jurassic and Cretaceous on the NCC [*Wang et al.*, 2005; *Wu et al.*, 2005; *Zhang et al.*, 2003] and its hybridized source of foundered crustal eclogite and cratonic lithosphere [*Gao et al.*, 2008, 2004]. However, the relatively long duration (~100 Myr) associated with the NCC reactivation was considered as an obstacle for the instability mechanism [*Menzies et al.*, 2007], because this time scale is significantly longer than expected for the lithospheric instability [e.g., *Duggen et al.*, 2005; *Molnar and Jones*, 2004]. It is important to note that the gravitational instability and subduction models are not mutually exclusive. For example, water delivered from subduction to the NCC may help weaken the lithosphere and lead to gravitational instability.

Although the gravitational instability for the NCC reactivation has been questioned for its time scales [*Menzies et al.*, 2007], most of our understanding on the instability has been derived from studies on noncratonic lithosphere without compositional buoyancy [e.g., *Conrad and Molnar*, 1997; *Houseman and Molnar*, 1997]. Gravitational instability of compositionally buoyant lithosphere was only investigated recently in laboratory studies with emphasis on instability conditions for Newtonian fluids [*Fourel et al.*, 2013; *Jaupart et al.*, 2007]. Important questions including the temporal and spatial scales for the instability of cratonic lithosphere remain unexplored [*Morency and Doin*, 2004]; also, the effect of various rheological properties (e.g., stress-dependent viscosity) has not been investigated [*Lenardic et al.*, 2003; *Wang et al.*, 2014]. Addressing these questions and their implications for the NCC reactivation is the main goal of this study.

2. Model Description

Lithospheric gravitational instability requires net negative buoyancy. Geochemistry studies suggest that melt depletion in cratonic lithosphere may result in 1–2.5% density reduction for the lithosphere [*Lee et al.*, 2011; *Poudjom Djomani et al.*, 2001; *Griffin et al.*, 2009]. However, there is no significant depth-variation in the degree of melt depletion and hence intrinsic density for individual cratonic lithosphere [*Carlson et al.*, 2005; *Lee et al.*, 2011], suggesting that the cold, top portion of cratonic lithosphere is gravitationally

© 2015. American Geophysical Union. All Rights Reserved.

Table 1. Physical Parameters

Box thickness $\boldsymbol{D}$	1250 km
Lithosphere thickness $\boldsymbol{d}$	250 km
Thermal expansivity α	3×10^{-5}/K
Reference density ρ_0	3300 kg/m^3
Gravitational acceleration $\boldsymbol{g}$	9.8 m/s^2
Reference temperature $\Delta \boldsymbol{T}$	750 K
Thermal diffusivity κ	1×10^{-6} m^2/s
Transition stress τ_T	0.5 MPa
Stress exponent $\boldsymbol{n}$	3.5

unstable, contrary to the isopycnic hypothesis [*Jordan*, 1978]. Joint seismic and petrologic analyses of peridotite xenoliths for the Kaapvaal Craton suggest that the lithosphere is negatively buoyant overall [*Schutt and Lesher*, 2010], consistent with other similar analyses [*Afonso et al.*, 2008]. Furthermore, the thermal boundary layer is thicker than compositional layer, thus providing extra negative buoyancy for cratonic lithosphere [*Cooper et al.*, 2004; *Lenardic et al.*, 2003].

We have formulated 2-D Cartesian thermochemical convection models to study the gravitational instability of chemically buoyant lithosphere. The basic model setup is similar to the laboratory studies by *Jaupart et al.* [2007]. The models include a thick (~250 km) top layer with smaller density and higher viscosity than the underlying bottom layer, analogous to cratonic mantle lithosphere overlying the mantle. Our models do not include the crust that does not have significant effect on the dynamics of cratonic lithosphere [*Beuchert et al.*, 2010; *Wang et al.*, 2014]. Assuming incompressible fluids with Boussinesq approximation, the nondimensional governing equations are described as the conservation of the mass, momentum, energy, and composition.

$$\nabla \cdot \mathbf{u} = 0, \tag{1}$$

$$-\nabla P + \nabla \cdot \left[\eta(\nabla \mathbf{u} + \nabla \mathbf{u}^T)\right] + Ra(T - BC)\mathbf{e_z} = 0, \tag{2}$$

$$\frac{\partial T}{\partial t} + \mathbf{u} \cdot \nabla T = \nabla^2 T, \tag{3}$$

$$\frac{\partial C}{\partial t} + \mathbf{u} \cdot \nabla C = 0, \tag{4}$$

where $\boldsymbol{u}$, P, η, and T are velocity vector, pressure, viscosity, and temperature, respectively; C represents the composition and C is 1 and 0 for the fluids in the top and bottom layers, respectively; $\boldsymbol{e_z}$ is the unit vector in vertical direction; and Ra and B are a Rayleigh number and compositional buoyancy number. The governing equations are obtained by using the following characteristic scales: length D, time D^2/κ, viscosity η_0, and temperature ΔT, where D is the thickness of the box, κ is the coefficient of thermal diffusivity, η_0 is the reference viscosity that is taken as the viscosity of the bottom layer, and ΔT is the temperature difference across the box. Ra and B are defined as

$$Ra = \frac{\alpha \rho_0 g \Delta T D^3}{\kappa \eta_0}, \tag{5}$$

$$B = \frac{\Delta \rho}{\rho_0 \alpha \Delta T}, \tag{6}$$

where α is the coefficient of thermal expansion, ρ_0 is the reference density, g is the gravitational acceleration, and $\Delta\rho$ is the intrinsic compositional density difference between the two layers. As suggested by laboratory studies [*Jaupart et al.*, 2007], the stability of the chemically buoyant top layer depends on both the buoyancy number B and the lithospheric Rayleigh number Ra_l

$$Ra_l = \frac{\alpha \rho_0 g \Delta T d^3}{\kappa \eta_l}, \tag{7}$$

where d is the lithospheric thickness and η_l is the lithospheric viscosity. All the relevant model parameters and their reference values are in Table 1.

We imposed no-slip boundary conditions at the surface and free-slip on all the other boundaries. The surface and bottom boundaries are isothermal, while along the side boundaries thermally insulating boundary conditions are used. The dimensionless temperatures are 0 and 1 for the top and bottom boundaries, respectively. Initially, the temperature increases linearly from 0 at the surface to 1 at the bottom of the cratonic lithosphere, and it is uniformly at 1 in the bottom layer. Superimposed on this temperature structure is a random temperature perturbation with a magnitude of 0.01. Notice that the top surface corresponds to

© 2015. American Geophysical Union. All Rights Reserved.

the crust-mantle boundary (i.e., Moho), and no-slip boundary condition is adequate for the Moho in cratonic settings where the temperature is relatively low. The isothermal boundary condition for the top surface represents a simplification of the Moho thermal state. The boundary conditions for the sidewall and bottom boundaries are more arbitrary, but these boundaries are more distant from the top layer and may not influence its gravitational instability. Notice that convective instability of cratonic lithosphere in our study does not depend on initial perturbation (neither wavelengths nor amplitude), unlike the Rayleigh-Taylor instability [e.g., *Houseman and Molnar*, 1997]. As to be shown in our numerical models, the instability of cratonic lithosphere does not start until after a long-time integration and when the mantle has developed active convection.

The rheology for cratonic lithosphere is poorly understood and is likely complicated with temperature, stress, and composition-dependent viscosity [*Lenardic and Moresi*, 1999; *Shapiro et al*., 1999; *Sleep*, 2003; *Pollack*, 1986; *Dixon et al*., 2004; *Wang et al*., 2014]. Melt depletion leads to not only compositional buoyancy but also low water and volatile content in cratonic mantle lithosphere [*Carlson et al*., 2005]. The reduced water and volatile content may lead to viscosity increase by a factor of 30–100 [*Pollack*, 1986; *Hirth and Kohlstedt*, 2003], or by as much as 3–4 orders of magnitude for cratonic lithosphere relative to asthenosphere, together with the temperature's effect [*Dixon et al*., 2004]. In numerical models, we employ simplified rheological models for both Newtonian and non-Newtonian rheologies. Our Newtonian models use two-layer viscosity structure, and for most cases the viscosity is $1000\eta_0$ and η_0 for the top and bottom layers, respectively. The top layer represents the cratonic lithosphere and its high viscosity reflects both composition and temperature-dependent viscosity. Another reason for using such two-layer viscosity structure is to enable direct comparison with the laboratory studies by *Jaupart et al*. [2007] that also used two-layer viscosity models.

For non-Newtonian models, we use a composite viscosity that incorporates both the Newtonian and non-Newtonian rheology [e.g., *Hirth and Kohlstedt*, 2003], and the effective viscosity is given by [e.g., *Podolefsky et al*., 2004]

$$\eta_{eff}=\frac{\eta_c}{1+\left(\frac{\eta_c\varepsilon}{\tau_T}\right)^{\frac{n-1}{n}}}, \tag{8}$$

where ε is the second invariant of strain rate tensor, τ_T and n are the transition stress and the stress exponent, respectively, and η_c reflects the composition and temperature-dependent viscosity to be discussed more later. The stress exponent is taken as 3.5 for dislocation creep as reported from laboratory experiments [e.g., *Hirth and Kohlstedt*, 2003] and commonly used in geodynamic studies [e.g., *Podolefsky et al*., 2004; *Wang et al*., 2014]. The transition stress could be in the range of 0.1–1 MPa in asthenospheric condition as suggested by *Hirth and Kohlstedt* [2003], but we use 0.5 MPa for transition stress here. Although these rheological parameters (i.e., n and τ_T) may vary and potentially affect the lithospheric instability, we do not attempt to address their effects in this study by keeping these parameters as constant. This expression of effective viscosity is consistent with experimental studies on the upper mantle rheology, i.e., the diffusion and dislocation creep mechanism dominate at low-stress and high-stress levels, respectively [e.g., *Hirth and Kohlstedt*, 2003]. In calculating lithospheric Rayleigh number Ra_l (i.e., equation (7)) for non-Newtonian models, the lithospheric viscosity is the averaged viscosity weighted by strain rate for cratonic lithosphere before the instabilities.

Although most of our non-Newtonian models use two-layer viscosity with two different η_c in equation (8) (i.e., $\eta_c=1000$ for cratonic lithosphere and $\eta_c=1$ for its underlying mantle), similar to the Newtonian models, the temperature and composition-dependent viscosity can be incorporated explicitly into η_c in a dimensionless form as

$$\eta_c=\eta_w exp\left(\frac{E}{T+T_{off}}-\frac{E}{1+T_{off}}\right), \tag{9}$$

where $E=E'/(R\Delta T)$ is dimensionless activation energy with R as the gas constant and E' as activation energy, $T_{off}=T_s/\Delta T$ is the normalized surface temperature with T_s as the surface temperature (i.e., Moho temperature here), and η_w is a pre-factor. It should be reiterated that our models use two-layer viscosity with $E=0$ and $\eta_w=\eta_c$, unless stated otherwise, for example, in discussion section where the temperature-dependent viscosity is explicitly explored.

© 2015. American Geophysical Union. All Rights Reserved.

These equations for thermochemical convection with composite rheology are solved using Citcom with a particle method [*McNamara and Zhong*, 2004; *Moresi et al*., 1996; *Tackley and King*, 2003]. Models are computed in a Cartesian box with an aspect ratio of 1–3. The model box consists of 128 by 128 elements for models with an aspect ratio of 1, and for models with an aspect ratio of 2 and 3 the number of elements in horizontal direction is proportionally increased. Initially, each element contains 16 tracers to represent the compositionally distinct cratonic lithosphere and the regular mantle. For all the cases, we compute the model until the entire top layer goes unstable or for a time corresponding to 4.5 Ga, whichever comes first. We use thermal diffusivity κ and box thickness D to define the time scaling D^2/κ.

3. Results

A total of 106 cases are computed with buoyancy number B varying from 0 to 0.9, Ra_l from $\sim$200 to 10^5, and Newtonian and non-Newtonian models (see Table 2 for all the non-Newtonian models). In this section, we will first present Newtonian and non-Newtonian models that are followed with models of different viscosity contrasts and aspect ratios.

3.1. Newtonian Models

Jaupart et al. [2007] performed laboratory studies on the gravitational instability of chemically buoyant lithosphere using Newtonian fluids in a setup that is similar to our numerical models. Their studies show that the instability is controlled by two parameters: buoyancy number B and lithospheric Rayleigh number Ra_l, and that depending on B and Ra_l, there are three possible instability regimes (Figure 2a). (1) In a stable regime for small Ra_l, the lithospheric layer remains stable for sufficiently long time (e.g., >4.5 Gyr) and convection only develops in the bottom layer. (2) In a layered convection regime for large Ra_l and $B \geq 0.5$ (Figure 2a), convection occurs separately in the top and bottom layers. (3) In an unstable regime for large Ra_l and small B (Figure 2a), lithospheric fluid sinks into the bottom layer. Figures 3a–3c show representative thermal and compositional fields from our 2-D models for stable, layered convection, and unstable regimes, respectively. The unstable regime includes an oscillatory unstable subregime for moderately large B, in which the destabilized fluid from the top layer moves up and down in the mantle (Figures 3d–3f) [*Fourel et al*., 2013; *Jaupart et al*., 2007].

Our 2-D Newtonian models agree remarkably well the laboratory work by *Jaupart et al*. [2007] (Figures 2b and 3). In our numerical modeling, a case falls in a stable regime if the lithosphere layer remains stable for >4.5 Ga. A stable top layer (i.e., lithosphere) requires small Ra_l or large lithospheric viscosity, consistent with previous studies [*Lenardic et al*., 2003; *Shapiro et al*., 1999]. However, when the lithospheric viscosity is reduced to lead to sufficiently large Ra_l, the top layer becomes unstable. Our numerical results suggest that the lithospheric instability only occurs for relatively small buoyancy number of $B \leq 0.4$ (Figure 2b), consistent with *Jaupart et al*. [2007] (Figures 2a and 2b). For cratonic lithosphere with 1–2.5% reduction in density [e.g., *Poudjom Djomani et al*., 2001], B is estimated in the range of 0.4–1.0, using the temperature difference across the lithospheric mantle at $\sim$750 K and thermal expansion at 3×10^{-5}/K (Table 1). A newly estimated density based on seismic and petrological studies suggests that B is $\sim$0.49 for the Kaapvaal Craton [*Schutt and Lesher*, 2010]. Therefore, the laboratory studies and our numerical results suggest that the gravitational instability of cratonic lithosphere that leads to replacement of mantle lithosphere by asthenosphere is unlikely to happen for Newtonian rheology.

3.2. Non-Newtonian Models

For non-Newtonian models, we observe the same three regimes as for Newtonian models, but these regimes occur in different parameter spaces of buoyancy number B and lithospheric Rayleigh number Ra_l (Figures 2b and 2c). We find that the lithospheric instability can happen for buoyancy number B up to 0.7 with the non-Newtonian rheology (Figure 2c). This is significantly larger than the threshold buoyancy number of $\sim$0.4 for the Newtonian rheology (Figure 2b) but is comparable with a range of buoyancy number estimated for cratonic lithosphere, thus making the lithospheric instability a possible mechanism for the reactivation of cratonic lithosphere. The instability also tends to occur at a larger Ra_l for the non-Newtonian rheology than for Newtonian rheology (Figures 2b and 2c), but this may partially be caused by the uncertainty in determining the temporally and spatially averaged lithospheric viscosity before the instability, which is required in calculating Ra_l. We also found that with non-Newtonian rheology the instability for

© 2015. American Geophysical Union. All Rights Reserved.

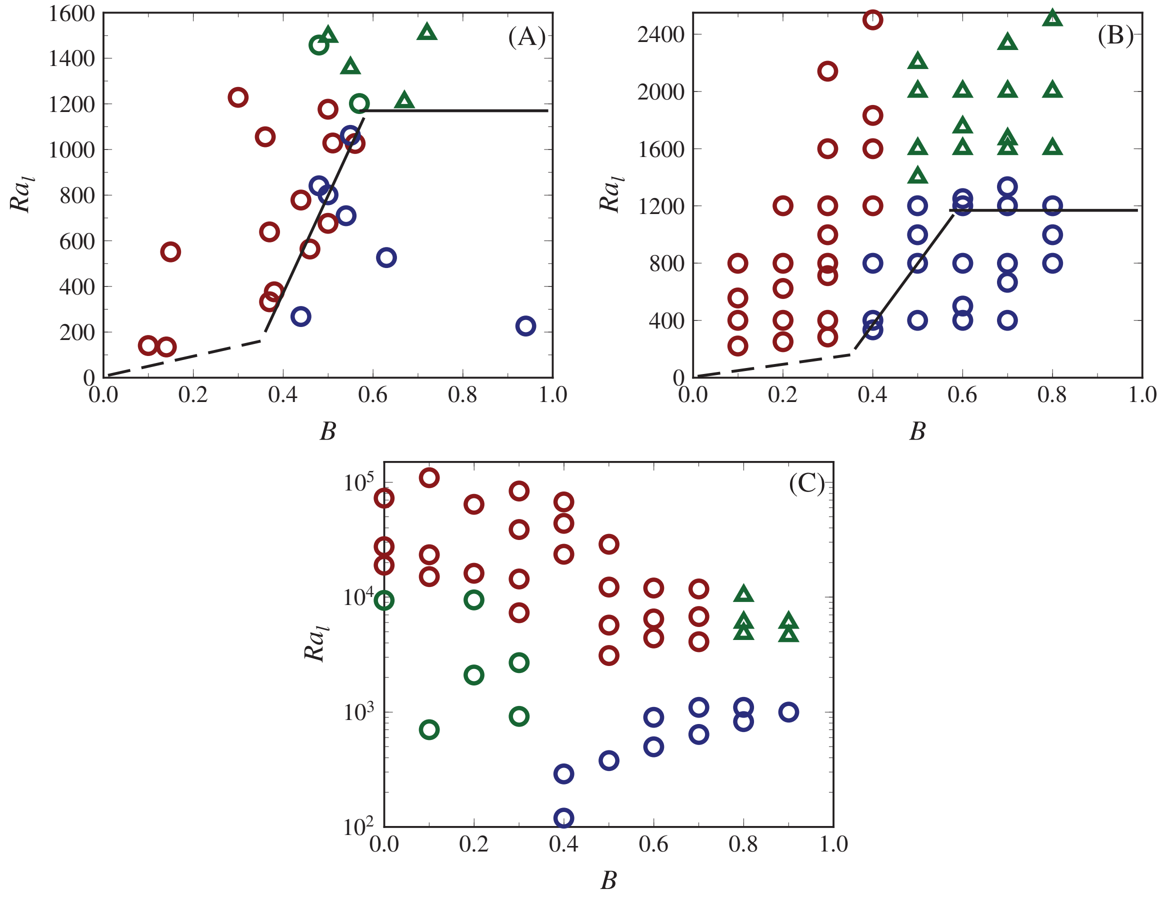

Figure 2. Different regimes of lithospheric instabilities depending on buoyancy number B and lithospheric Rayleigh number Ra_l from (a) laboratory studies for Newtonian fluids by *Jaupart et al*. [2007], (b) Newtonian models, and (c) non-Newtonian models. Red circles, blue circles, and green triangles are for unstable, stable, and layered convection regimes. In Figure 2a, the green circles correspond to uncertain cases in *Jaupart et al*. [2007], and the black lines were from their stability analyses (also plotted in Figure 2b). The green circles in Figure 2c correspond to cases with mantle viscosities greater than 10^{21} Pa s (listed in Table 2) which are considered too high and are excluded in Figure 5b for the instability times.

cratonic lithosphere (i.e., $B \geq 0.5$) is episodic and consists of multiple events each of which has a relatively small horizontal length scale and only affects a small segment of the lithosphere.

The larger threshold buoyancy number $B \sim 0.7$ with the non-Newtonian rheology and the episodic and multistaged instability process for cratonic lithosphere are inherently related to each other and are caused by the dynamic interaction between buoyancy structure and non-Newtonian rheology. Here we use a representative and reference non-Newtonian model (CaseNN026 in Table 2 with $B = 0.5$ and $Ra_l = 5700$) to describe the episodic and multistaged instability process and its characteristic time and length scales. For the reference case, with the given initial temperature, the thermal boundary layer thickens with time at early stage and becomes thicker than the compositionally buoyant top layer. The thickening top thermal boundary layer drives thermal convection in the bottom layer, while the top layer remains stable (Figure 4a). With time, a segment of the top layer with a width of ~300 km (or ~0.3 in dimensionless width) becomes unstable, forming a blob that sinks into the bottom layer (Figure 4b). Subsequently, another part of the top layer goes unstable and sinks into the bottom layer (Figure 4d), and the process continues in multiple stages to affect the entire top layer (Figure 4f). The total time for this multistaged instability is on the order of tens of Myr (Figures 4b–4f), if the time is scaled using the model parameters in Table 1.

The total time of the instability affecting the entire top layer of dimensionless width of 1 (or 1250 km) can be determined from the time-dependent averaged flow velocity of the top layer, V_{rms}, and the cumulative fraction of lithospheric materials (i.e., $C = 1$ fluid) that have traveled across a dimensionless depth of 0.2 (or 250 km) to the bottom layer C_d (Figure 5a). The spikes in the flow velocity V_{rms} indicate episodic, multistaged instability events at different times (Figure 4), which cause the stair-step increase in C_d (i.e., the

© 2015. American Geophysical Union. All Rights Reserved.

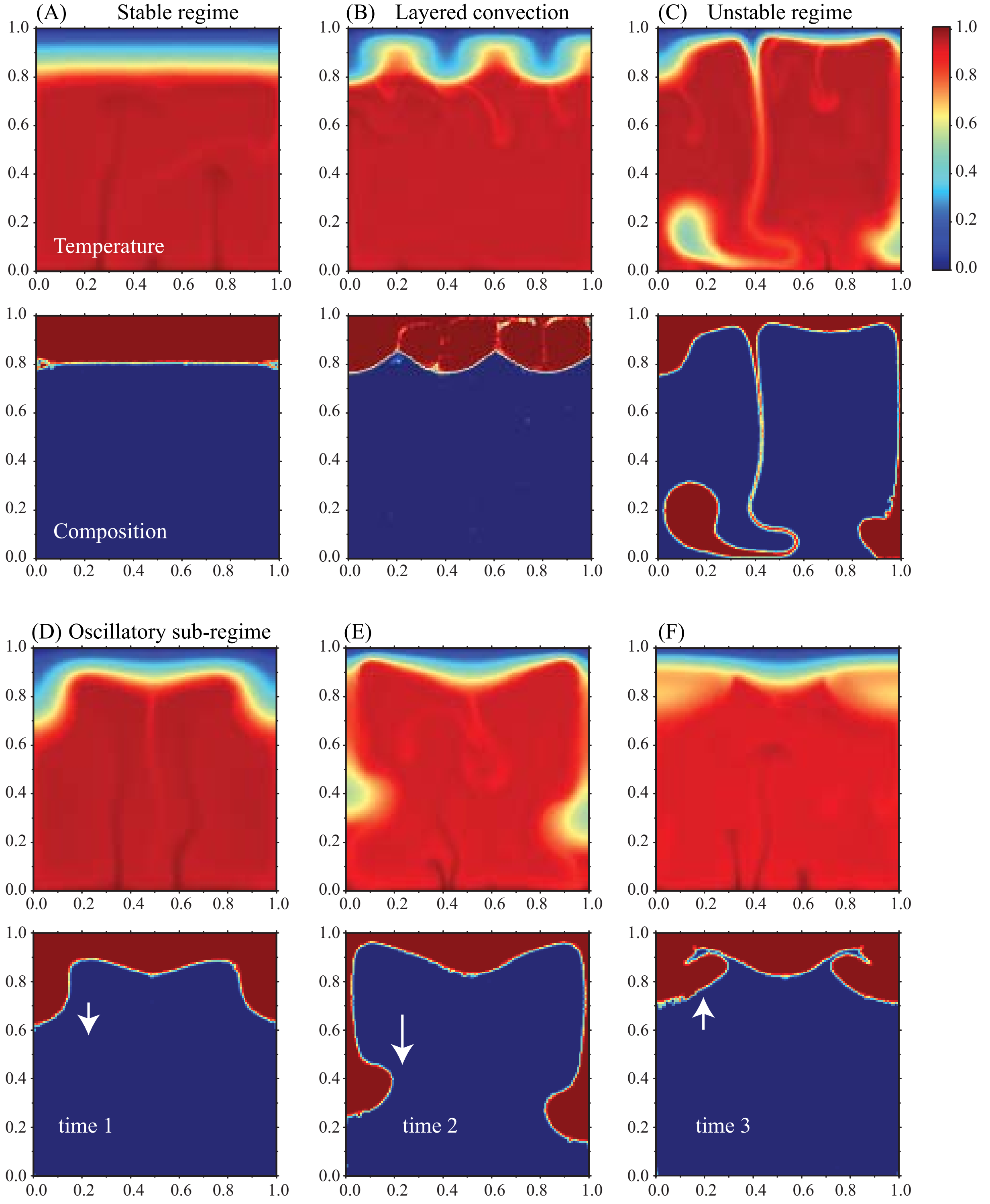

Figure 3. Snapshots of temperature (the upper row) and compositional (the lower row) fields of four Newtonian models to display the instability regimes: (a) stable regime, (b) layered convection, (c) unstable regime, and (d)–(f) for the oscillatory subregime at three different times. The red and blue in compositional fields represent the cratonic lithosphere and regular mantle materials, respectively. The arrows in Figures 3d–3f represent the directions of the flow.

cumulative fraction) (Figure 5a). An onset time of the instability is defined as when V_{rms} first surpasses 1% of its maximum (the first circle in Figure 5a). The total instability time is defined as the time from the onset to when the cumulative fraction C_d reaches an approximately constant value and the entire horizontal extent

© 2015. American Geophysical Union. All Rights Reserved.

Table 2. Model Parameters and Results for Non-Newtonian Models

Case	γ[a]	B	Ra_i[b]	Ra_l[b]	t_{dlm}[c] (Myr)	$<T_{blob}>$[d] (×750°C)	η_l[d] (×10^{21} Pa s)	η_m[d] (×10^{21} Pa s)
NN001	1,000	0	1e5	9,400	11.6	0.57	1.4 ± 12.1	2.3 ± 0.77
NN002	1,000	0	4e5	27,500	1.4	0.60	0.48 ± 2.8	0.48 ± 0.19
NN003	1,000	0	8e5	18,900	1.0	0.65	0.7 ± 8.6	0.60 ± 0.09
NN004	1,000	0	1e6	72,700	2.0	0.63	0.18 ± 3.1	0.30 ± 0.11
NN005	1,000	0.1	1e5	700	20.8	0.56	19.0 ± 12.8	2.2 ± 0.48
NN006	1,000	0.1	3e5	23,500	6.0	0.54	0.57 ± 4.3	0.83 ± 0.35
NN007	1,000	0.1	1e6	15,100	6.1	0.57	0.88 ± 1.3	0.35 ± 0.03
NN008	1,000	0.1	2e6	1.1e+05	1.1	0.59	0.12 ± 1.3	0.17 ± 0.06
NN009	1,000	0.2	1e5	2,100	126.1	0.53	6.3 ± 0.48	2.04 ± 0.32
NN010	1,000	0.2	3e5	9,500	29.4	0.52	1.4 ± 4.3	1.2 ± 0.23
NN011	1,000	0.2	8e5	16,100	12.8	0.57	0.82 ± 0.73	0.69 ± 0.04
NN012	1,000	0.2	2e6	64,500	4.1	0.55	0.21 ± 1.6	0.23 ± 0.09
NN013	1,000	0.3	1e5	920	286.2	0.50	14.4 ± 1.9	3.7 ± 0.12
NN014	1,000	0.3	3e5	2,700	110.7	0.52	4.9 ± 4.9	1.7 ± 0.32
NN015	1,000	0.3	1e6	7,300	49.4	0.51	1.8 ± 1.6	0.53 ± 0.09
NN016	1,000	0.3	2e6	14,400	31.3	0.51	0.92 ± 2.1	0.32 ± 0.06
NN017	1,000	0.3	6e6	38,800	8.1	0.53	0.34 ± 1.1	0.10 ± 0.03
NN018	1,000	0.3	1e7	84,300	8.3	0.52	0.16 ± 0.80	0.088 ± 0.03
NN019	1,000	0.4	8e5	120	Stable		114 ± 55	2.8 ± 0.72
NN020	1,000	0.4	2e6	290	Stable		46.4 ± 32.0	0.49 ± 0.11
NN021	1,000	0.4	6e6	23,700	98.7	0.45	0.56 ± 1.2	0.25 ± 0.004
NN022	1,000	0.4	3e7	43,700	14	0.42	0.30 ± 0.62	0.034 ± 0.003
NN023	1,000	0.4	4e7	67,700	13.4	0.43	0.20 ± 0.97	0.026 ± 0.002
NN024	1,000	0.5	4e6	380	Stable		35.2 ± 15.2	0.24 ± 0.05
NN025	1,000	0.5	8e6	3,100	124.6	0.37	4.3 ± 0.58	0.13 ± 0.01
NN026	1,000	0.5	2e7	5,700	62.1	0.37	2.3 ± 1.0	0.063 ± 0.002
NN027	1,000	0.5	4e7	12,200	43.9	0.36	1.1 ± 0.74	0.028 ± 0.001
NN028	1,000	0.5	6e7	29,000	18.6	0.37	0.46 ± 0.48	0.018 ± 0
NN029	1,000	0.6	8e6	500	Stable		26.4 ± 10.1	0.11 ± 0.02
NN030	1,000	0.6	2e7	900	Stable		14.2 ± 2.6	0.059 ± 0.008
NN031	1,000	0.6	2.2e7	4,400	96.7	0.31	3.0 ± 0.35	0.048 ± 0.004
NN032	1,000	0.6	3e7	6,500	45.6	0.33	2.1 ± 0.095	0.032 ± 0.002
NN033	1,000	0.6	6e7	12,000	22.0	0.33	1.1 ± 0.27	0.017 ± 0
NN034	1,000	0.7	8e6	640	Stable		20.8 ± 5.5	0.13 ± 0.021
NN035	1,000	0.7	2e7	1,100	Stable		12.2 ± 3.6	0.052 ± 0.007
NN036	1,000	0.7	2.5e7	4,100	83.5	0.27	3.2 ± 0.66	0.048 ± 0.004
NN037	1,000	0.7	4e7	6,800	40.8	0.28	2.0 ± 0.28	0.03 ± 0.001
NN038	1,000	0.7	8e7	11,800	21.8	0.29	1.1 ± 0.4	0.014 ± 0
NN039	1,000	0.8	8e6	830	Stable		15.9 ± 11.2	0.12 ± 0.018
NN040	1,000	0.8	2e7	1,100	Stable		11.9 ± 3.7	0.046 ± 0.006
NN041	1,000	0.8	3e7	4,800	Layered		2.7 ± 0.55	0.037 ± 0.001
NN042	1,000	0.8	4e7	6,000	Layered		2.2 ± 0.51	0.026 ± 0
NN043	1,000	0.8	8e7	10,300	Layered		1.3 ± 0.48	0.016 ± 0
NN044	1,000	0.9	2e7	1,000	Stable		13.4 ± 3.9	0.049 ± 0.007
NN045	1,000	0.9	3e7	4,600	Layered		2.9 ± 0.34	0.037 ± 0
NN046	1,000	0.9	4e7	6,000	Layered		2.2 ± 0.7	0.03 ± 0.002
NN047	300	0.5	2e7	27,500	20		0.48 ± 0.27	0.049 ± 0.001
NN048	100	0.5	2e7	70,000	6		0.19 ± 0.25	0.041 ± 0.001
NN049	30	0.5	2e7	3.5e5	1.43		0.038 ± 0.72	0.078 ± 0.006
NN050	10	0.5	2e7	4.9e5	0.49		0.027 ± 0.36	0.078 ± 0.005
NN051	300	0.5	6e6	8,400	85		1.6 ± 0.13	0.085 ± 0.003
NN052	100	0.5	2e6	6,000	63		2.2 ± 0.70	0.26 ± 0.022
NN053	30	0.5	6e5	7,500	98		1.8 ± 5.8	1.24 ± 0.40
NN054	10	0.5	2e5	25,200	20.8		0.53 ± 2.7	1.69 ± 1.0
NN055[e]	1,000	0.5	2e7	9,700	117		1.4 ± 0.68	0.047 ± 0.002
NN056[f]	1,000	0.5	2e7	6,300	162.5		2.1 ± 0.45	0.057 ± 0.005

[a] γ is the viscosity contrast between the top and bottom layers as in equation (8).

[b] Ra_i is the input Rayleigh number that is defined by box depth and a mantle viscosity. 1e5 reads as 10^5. Ra_l is the lithospheric Rayleigh number from equation (7) with lithospheric viscosity determined from an average viscosity weighted by strain rate over the whole lithosphere before the instability.

[c] t_{dlm} is the total instability time in Myr. Cases with stable lithosphere or layered convection do not have instability times.

[d] $<T_{blob}>$ is the averaged temperature for destabilized blobs that is only defined for cases with unstable lithosphere. η_l and η_m are averaged lithospheric and mantle viscosities, respectively, and their standard deviations are also given.

[e] This is the case that has an aspect ratio of 2.

[f] This is the case that has an aspect ratio of 3.

© 2015. American Geophysical Union. All Rights Reserved.

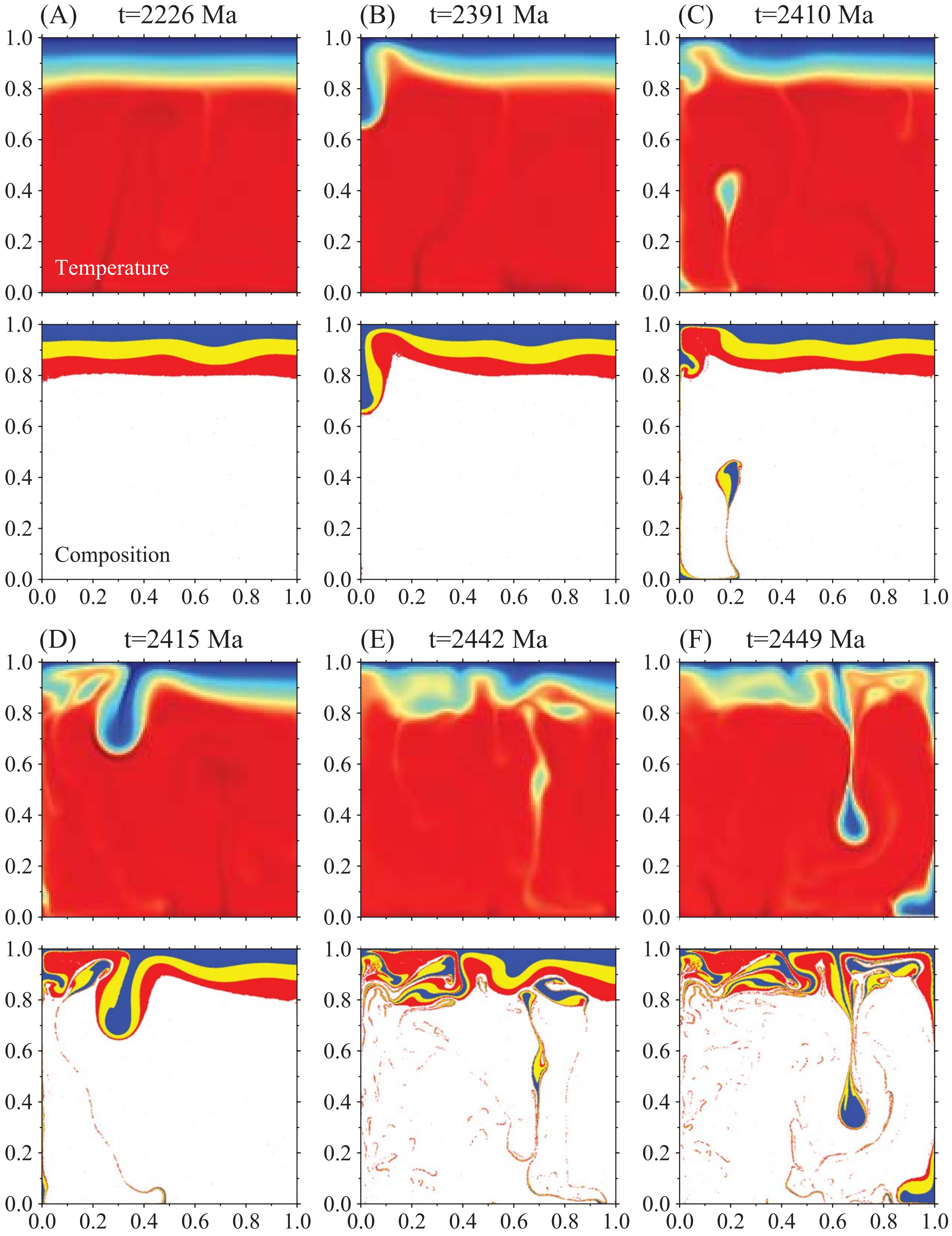

Figure 4. Snapshots of temperature (the upper row) and composition (the lower row) for a representative non-Newtonian case (Case NN026 in Table 2) at six different time steps. The color scale bar is for dimensionless temperature. In the composition plots, the white color is for the bottom layer (i.e., the normal mantle with $C = 0$), while the top layer is represented by three layers of different colors with blue, yellow, and red for initially shallow, middle, and large depths, respectively. Note that these three color layers have the same composition $C = 1$ and intrinsic density.

© 2015. American Geophysical Union. All Rights Reserved.

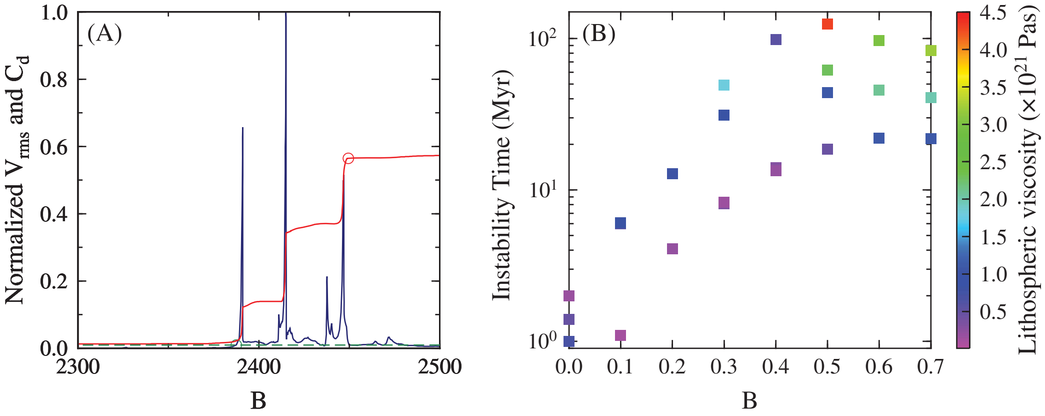

Figure 5. (a) Time dependences of normalized root mean square flow velocity for the lithosphere V_{RMS} (blue) and the cumulative fraction of lithospheric materials (i.e., $C = 1$ fluid) that have traveled across a dimensionless depth of 0.2 (or 250 km) to the bottom layer C_d (red) for case NN026. (b) Total instability times versus buoyancy number B for non-Newtonian cases in unstable regime (Table 2) that have the mantle viscosity less than 10^{21} Pa s. The lithospheric viscosity for each case is color coded in Figure 5b. The green and red circles in Figure 5a denote the onset and end of the instability process.

of the top layer has been destabilized (the second circle in Figure 5a). The total instability time was estimated to be ~60 Myr for the reference case (Figure 5a and Table 2).

Such defined total instability time generally increases with increasing buoyancy number B but decreases with increasing lithospheric Ra_l (or decreasing lithospheric viscosity) (Figure 5b and Table 2). For $B = 0$ (i.e., noncratonic lithosphere), the instability happens over a short time of 1–2 Myr (Table 2), consistent with previous studies for noncratonic lithosphere [e.g., *Molnar and Jones*, 2004]. It generally takes one or two instability events to remove most of the top layer of $C = 1$ fluid (Figure 6a). However, for cratonic lithosphere with $B > 0.4$, it may take multiple stages of instability to affect the entire top layer (~1200 km wide) over time scales of ~100 Myr for relatively small Ra_l.

The increased total time and multiple stages of instability for cratonic lithosphere (i.e., $B > 0.4$) are related to the lithospheric buoyancy structure and the length scale of instability. The net negative buoyancy driving the instability resides in the cold and shallow part of the compositionally buoyant top layer, and this may have two consequences. First, because the thickness of the upper layer with net negative buoyancy controls the length scale of the instability [*Jaupart et al.*, 2007] and because this layer thins with increasing B, this results in a reduced length scale of the instability with increasing B (Figures 4c–6a for $B = 0$, 0.3, and 0.5, respectively). Consequently, it takes more instability events and longer time to destabilize the whole top layer with a larger B (Figure 5b). Figure 7a shows the wavelength (i.e., length scale) of the initial instability for models with different B and Ra_l and confirms that B has the first-order control on the instability length scale that decreases with increasing B. Here the wavelength of the initial instability (i.e., at onset time) is determined by quantifying the horizontal length scale of instability-induced temperature variation near the bottom of the cratonic layer. Second, because the instability requires thermal buoyancy of sinking blobs to overcome their compositional buoyancy, the blobs for cases with larger B should be colder and come from shallower depths. This is confirmed by the blob's temperatures versus B (Figure 7b) and the shallower initial depths of sinking materials with larger B (Figures 6a, 6b, and 4 for $B = 0$, 0.3, and 0.5, respectively). These blob's temperatures are determined by computing an average temperature of destabilized cratonic materials (i.e., with $C = 1$) between the nondimensional depths of 0.2 and 0.3 at the time when the head of the first sinking blob has reached a depth of 0.3. In general, for $B = 0$ (i.e., noncratonic lithosphere), the instability affects mostly the deep part of the lithosphere with relatively large horizontal length scale, while the shallow part of the lithosphere is largely unaffected (Figure 6a). However, for $B > 0.4$ (i.e., cratonic lithosphere), the instability occurs at relatively short length scale and destabilizes the shallow part of the lithosphere where the net negative buoyancy is sufficiently large to cause the instability (Figure 4d).

We now come back to illustrate the cause for the increased threshold buoyancy number for instability for non-Newtonian models ($B \sim 0.7$), relative to that for Newtonian models ($B \sim 0.4$) (Figures 2b and 2c). The destabilized blobs for Newtonian models are always warmer than their non-Newtonian counterparts for given

© 2015. American Geophysical Union. All Rights Reserved.

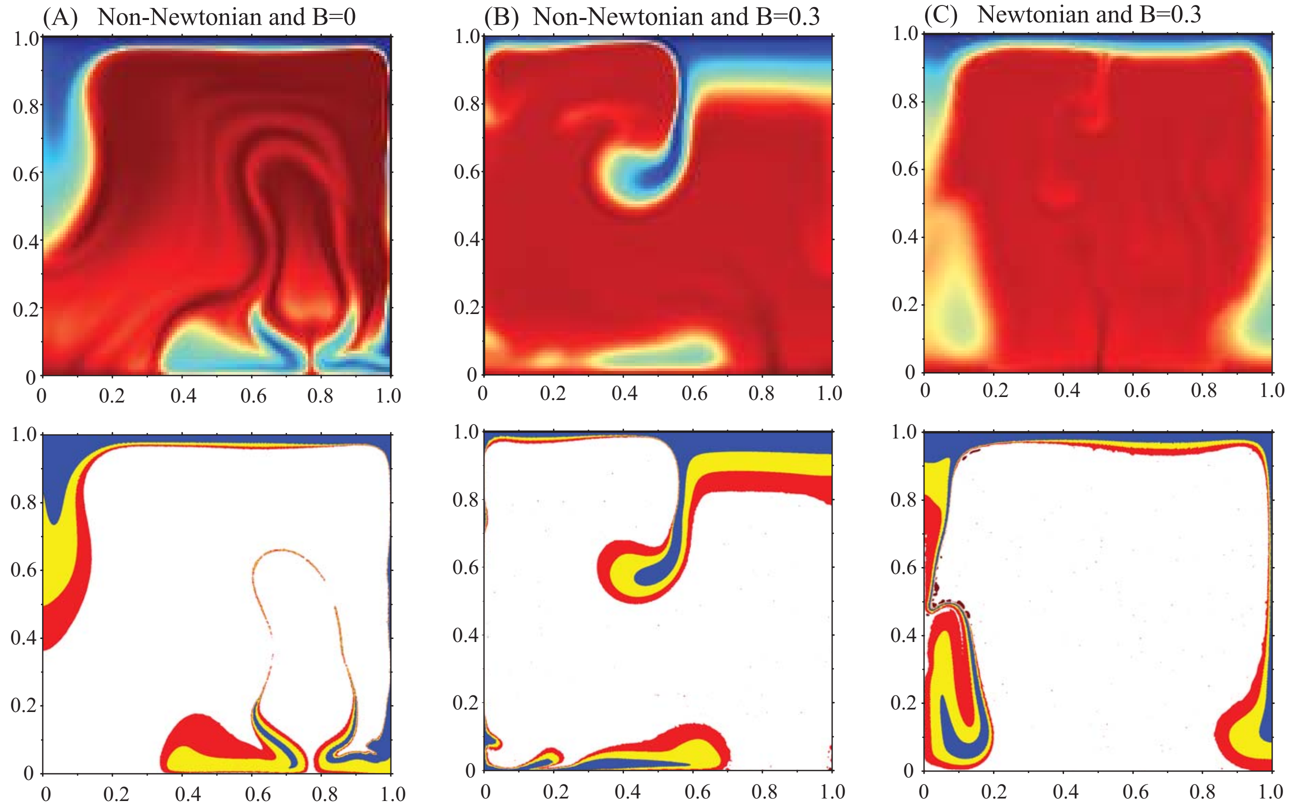

Figure 6. Snapshots of temperature (the upper row) and composition (the lower row) for (a) non-Newtonian model with $B = 0$ and $Ra_l = 18{,}900$ (Case NN003), (b) non-Newtonian model with $B = 0.3$ and $Ra_l = 7300$ (Case NN015), and (c) Newtonian model with $B = 0.3$ and $Ra_l = 1000$.

buoyancy number B (Figure 7b). Furthermore, the instability for Newtonian models tends to remove mostly the warmer, lower part of the top layer (Figure 6c for $B = 0.3$ and Newtonian rheology), which is consistent with the relatively larger temperatures for the blobs in Newtonian models (Figure 7b). This suggests that the destabilized blobs in Newtonian models are not as negatively buoyant as those in non-Newtonian models.

However, it is the localized deformation from non-Newtonian rheology that is responsible for the difference in the blobs' temperature and buoyancy (i.e., the threshold buoyancy number) between non-Newtonian

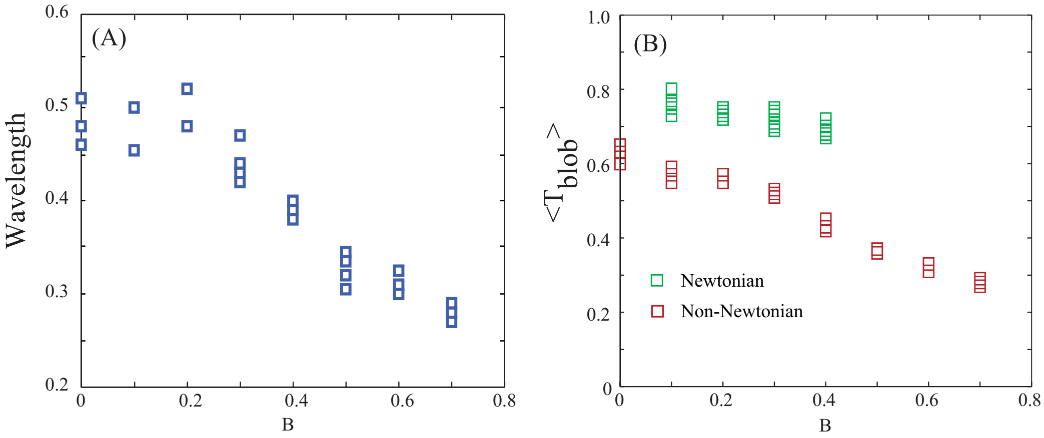

Figure 7. (a) Dimensionless horizontal length scale (i.e., wavelengths) for instability versus buoyancy number B for non-Newtonian cases in unstable regime with sublithospheric mantle viscosity $<10^{21}$ Pa s. (b) Averaged dimensionless temperature of the destabilized blobs versus B for Newtonian (green squares) and non-Newtonian (red squares) cases with different Ra_l. The instability wavelengths and blob temperatures are computed around the onset times.

© 2015. American Geophysical Union. All Rights Reserved.

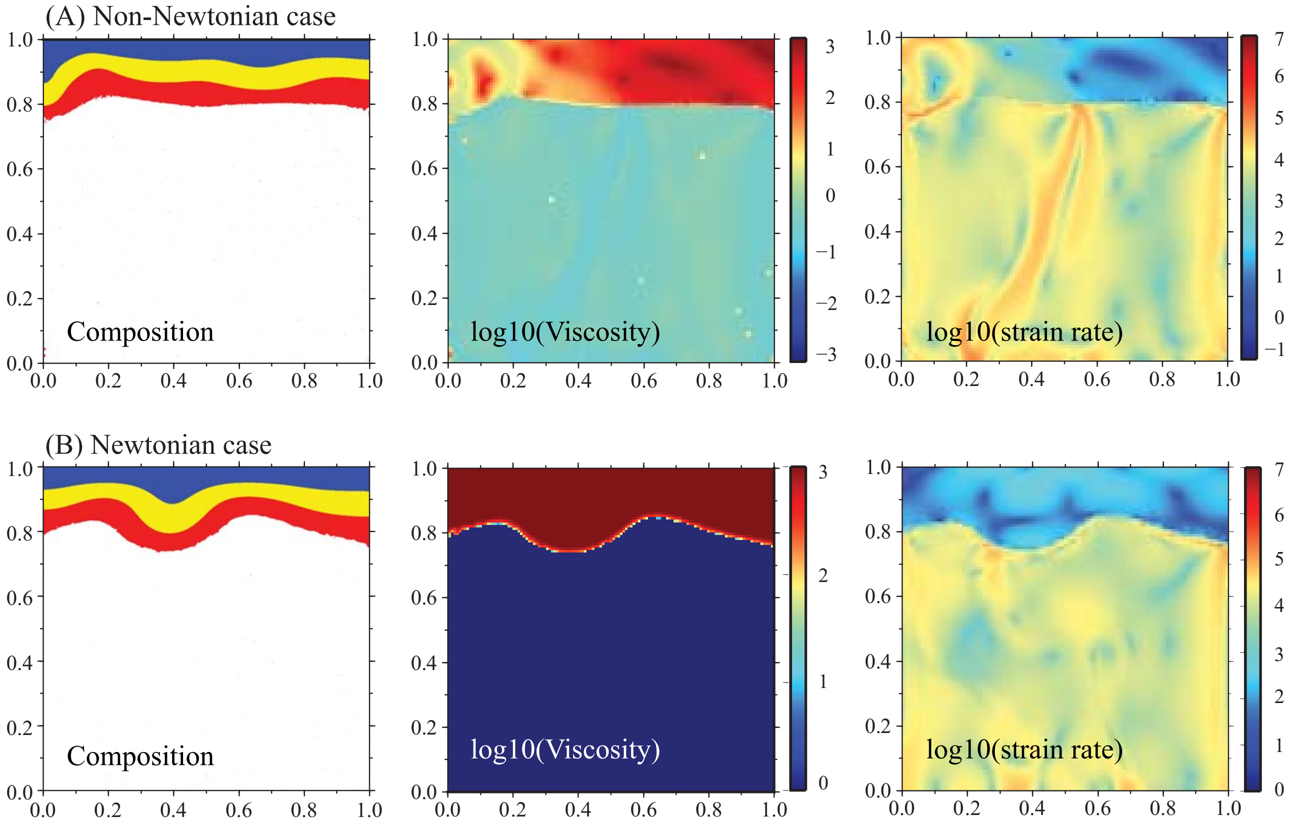

Figure 8. Snapshots of composition (left), viscosity (middle), and strain rate (right) for (a) case NN026 and for (b) Newtonian case with $B = 0.3$ and $Ra_l = 1000$ both at the onset time. The dimensionless viscosity and strain rate are in the logarithmic scale.

and Newtonian models. Non-Newtonian rheology weakens the regions with large stresses and decouples efficiently regions with large stresses from that with small stresses. These regions with large stresses are mostly initiated at the shallowest part of the top layer with the largest negative buoyancy. This is sometimes referred to as localized deformation effect that is best demonstrated with a snapshot of effective viscosity and strain rate at about onset of instability for the reference non-Newtonian case (NN026) (Figure 8a). The sinking blob is associated with large strain rate and is surrounded by regions of reduced effective viscosity that separate and decouple the blob from the rest of the lithosphere. However, for Newtonian models with uniform viscosity, the flow is uniformly coupled and the strain rate in the top layer does not vary significantly (Figure 8b). The localized deformation effect helps tap colder, shallower, and more negatively buoyant materials ($C = 1$ fluid) to drive the instability so that it can occur for lithosphere with a larger buoyancy number B in non-Newtonian models than in Newtonian models. We also noticed that the episodic and multistaged instability only happens in non-Newtonian models with large buoyancy number, and for Newtonian models the instability occurs simultaneously in different parts of the top layer (Figure 6c), suggesting that the localized deformation from non-Newtonian rheology plays an essential role in lithospheric deformation.

Finally, it is interesting to note some distinct characteristics in thermal and chemical mixings during the instability process for cratonic lithosphere with a large buoyancy number. For example, for the reference non-Newtonian case, not all the compositionally buoyant materials (i.e., $C = 1$ fluid) sink into the bottom layer, as seen in the cumulative fraction C_d that is significantly less than 1 at the end of the instability ($C_d \sim 0.57$ in Figure 5a). That is, after the onset of instability a significant fraction of $C = 1$ fluid moves, circulates, and mixes within the top layer but never sinks below a dimensionless depth of 0.2 into the bottom layer (e.g., Figure 4f). Some of the $C = 1$ fluid comes back to the top layer after sinking into the bottom layer and mixing with the $C = 0$ fluid there (Figure 4e–f). At the end of the instability, while the top layer is mixed

© 2015. American Geophysical Union. All Rights Reserved.

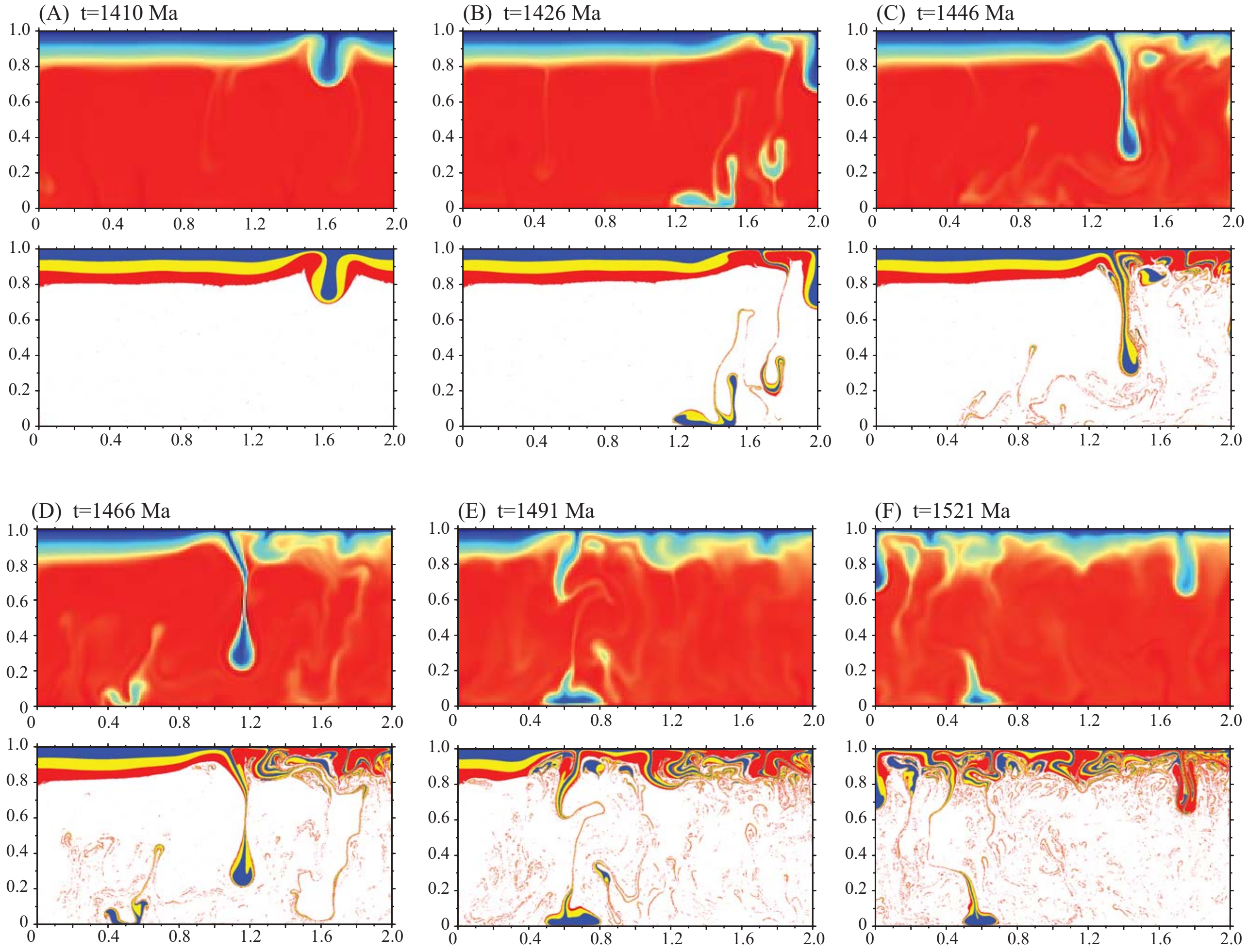

Figure 9. Snapshots of temperature (the upper row) and composition (the lower row) at six different time steps for a non-Newtonian model (case NN055) with $B = 0.5$, $Ra_l = 9700$ and an aspect ratio of 2.

thoroughly thermally (i.e., the top layer is significantly heated and has a thin thermal boundary layer) and reasonably well chemically, it still contains dominantly $C = 1$ fluid (Figure 4f).

3.3. Effects of Different Box Aspect Ratio and Viscosity Contrasts

All the results presented so far have been from models with a unit aspect ratio and a viscosity ratio of 10^3 between lithosphere and the underlying mantle (i.e., equation (8)). We also calculated two models with an aspect ratio of 2 and 3 (Cases NN055 and NN056 in Table 2) to examine possible effects of the aspect ratio on our results. Case NN055 has the same input parameters as that for the reference case (Case NN026) except for an aspect ratio of 2. Notice that although input Rayleigh numbers are the same for these two cases, Ra_l for Case NN055 is larger than that for Case NN026 (Table 2). This is because the averaged lithospheric viscosity before the onset for Case NN055 is smaller than that for Case NN026. As shown in Figure 9, with the increased aspect ratio, the lithospheric instability shows same episodic and multistaged behaviors as in Case NN026 with the instability propagating from one side of the box to the other. We also found that it takes about ∼60 and 117 Myr to destabilize the top layer for half of the box and the entire box, respectively (Figure 9 and Table 2). These instability times are generally consistent with that for Case NN026 (Figure 5a and Table 2).

Case NN056 is identical to cases NN026 and NN051 (Table 2) except for an aspect ratio of 3. For case NN056, the instability shows again the same episodic and multistaged behavior as in the other two cases. It takes ∼57 Myr to destabilize the first one third (i.e., dimensionless length of 1) of the lithosphere and ∼162

© 2015. American Geophysical Union. All Rights Reserved.

Myr for the entire length of the lithosphere (Table 2). These results suggest that irrespective of the aspect ratio of model box, the total instability time that is required to destabilize the cratonic lithosphere of the same horizontal length scale of ~1200 km (or dimensionless length 1) is nearly the same. We also observe that for case NN056 the instability does not always propagate from one side of the box to the other. After the first one third of the box is destabilized, another instability develops at the center of the stable part of the lithosphere. These two instabilities eventually destabilize the whole box, leading to a slightly shorter instability time of ~162 Myr than expected for this case with an aspect ratio 3. These results suggest that the aspect ratio of the box does not significantly affect the temporal and spatial scales and style of the instability.

Jaupart et al. [2007] indicated that for Newtonian fluids, the instability of chemically buoyant lithosphere is insensitive to the viscosity ratio between lithosphere and the underlying mantle. However, it is unclear whether this statement is equally true for non-Newtonian fluids. Here we use two sets of non-Newtonian models with different viscosity ratios to investigate possible effects of viscosity contrast. All these models have buoyancy number $B = 0.5$. The first set includes cases NN026 and NN047–050 (Table 2) that have the same input Rayleigh number (or the same mantle viscosity), but different viscosity ratios of 1000, 300, 100, 30, and 10, respectively. Notice that a larger viscosity ratio implies a larger lithospheric viscosity or smaller Ra_l for these cases (Table 2). The total instability times are 62, 20, 6, 1.43, and 0.5 Myr for cases NN026 and NN047–050 (Table 2), respectively. This is generally consistent with what we have proposed that the total instability time is controlled mainly by lithospheric viscosity and is insensitive to the viscosity of the lower layer.

The second set consists of cases NN026 and NN051–054, for which the input Rayleigh number decreases proportionally as the viscosity contrast decreases from 1000 to 300, 100, 30, and 10, respectively (Table 2). We may interpret this set of cases as having approximately the same lithospheric viscosity but different mantle viscosity (i.e., a larger mantle viscosity with a smaller viscosity ratio). The total instability times for cases NN026, NN051, and NN052 with viscosity ratio of 1000, 300, and 100 do not differ significantly (Table 2), but the times for cases NN053 and NN054 with viscosity ratio of 30 and 10 seem to differ more from other cases in this set (Table 2). However, we notice that for these last two cases with smallest viscosity ratios, the mantle viscosity exceeds 10^{21} Pa s and is also higher than the averaged lithospheric viscosity, both of which seem unrealistic. Additionally, the instability for these two cases seems to have larger horizontal scale with less episodic events. In summary, we think that the viscosity ratio does not affect the results significantly, provided that the effective lithospheric viscosity is larger than the mantle viscosity.

4. Discussion

4.1. Style and Temporal and Spatial Scales of Lithospheric Instability

Gravitational instability of lithosphere is considered as an important process affecting continental magmatism/volcanism and tectonics [e.g., *Elkins-Tanton*, 2007; *Molnar and Jones*, 2004]. A large number of studies have investigated the dynamics of the instability for chemically neutrally buoyant lithosphere (i.e., buoyancy number $B = 0$) with Newtonian and non-Newtonian rheology [e.g., *Conrad and Molnar*, 1997; *Harig et al*., 2010; *Houseman and Molnar*, 1997]. However, geochemical studies suggest that all the continental lithosphere is chemically buoyant to some extent relative to its underlying mantle [e.g., *Lee et al*., 2011]. The instability of chemically buoyant lithosphere was only recently investigated in laboratory studies for Newtonian fluids. *Jaupart et al*. [2007] reported that for Newtonian rheology lithospheric instability occurs for buoyancy number $B \leq 0.4$, suggesting that the instability may not happen for cratonic lithosphere with B ranging between 0.4 and 1. However, our numerical modeling, while reproducing the laboratory work by *Jaupart et al*. [2007] for Newtonian fluids, shows that lithospheric instability may occur for B up to 0.7 with non-Newtonian rheology (Figures 2b and 2c), suggesting that non-Newtonian rheology may play a key role in the instability of cratonic lithosphere.

The non-Newtonian rheology leads to other distinct features for instability of cratonic lithosphere (i.e., $B > 0.4$). The instability happens to the shallow part of the lithosphere with relatively short horizontal length scales (Figures 4 and 7a), which differs significantly from the instability for Newtonian fluids or chemically neutrally buoyant lithosphere that removes mostly the bottom of the lithosphere [e.g., *Conrad and Molnar*, 1999; *Jaupart et al*., 2007]. This also differs from convective entrainment in thermochemical convection

© 2015. American Geophysical Union. All Rights Reserved.

models that erode and destruct gradually cratonic lithosphere from the bottom of cratonic lithosphere upward [*Beuchert et al*., 2010; *Lenardic and Moresi*, 1999; *Shapiro et al*., 1999; *Wang et al*., 2014]. These distinct features and the increased threshold buoyancy number up to 0.7 can be explained by dynamic interaction between the buoyancy structure and non-Newtonian rheology. With a relatively large *B*, the net negative buoyancy driving the instability only exists in the cold, shallow part of the lithosphere. The negative buoyancy induces stress variations that cause weakening in high-stress regions with non-Newtonian rheology and decoupling there (Figure 8a), thus enabling the instability to grow locally at relatively small length scales.

With the Newtonian rheology the fluids are uniformly coupled together, the net negative buoyancy at the shallow depths for cratonic lithosphere with large buoyancy number would not be able to go unstable by itself. Therefore, the threshold buoyancy number for instability is smaller for Newtonian rheology than that for non-Newtonian rheology. When the buoyancy number is relatively small (i.e., noncratonic lithosphere), net negative buoyancy exists over a large depth range in the lithosphere, and consequently the instability occurs over large vertical and horizontal scales (Figure 7a). Lithospheric instability at larger spatial scales for smaller buoyancy number also implies that destabilized blobs on average are warmer (Figure 7b).

The intrinsically small horizontal length scale for instability of cratonic lithosphere (i.e., $B > 0.5$) with non-Newtonian rheology suggests that on a regional scale for cratonic lithosphere of horizontal length scale of $\sim$1000 km or more, the instability is episodic and consists of multiple events that may last for $\sim$100 Myr to destabilize the whole lithosphere (Figures 4 and 5). It should be pointed out that the total instability time is mainly controlled by effective lithospheric viscosity and buoyancy number (i.e., intrinsic density of cratonic lithosphere) (Figure 5). Although the depth of the box, as the length scale, is used to scale the time, the relevant length scale would be the lithospheric thickness. Our current study did not explore the effect of lithospheric thickness, but because our models use a representative reference thickness of 250 km, the estimated instability time should be relevant and applicable to observations. Different rheological parameters including power law exponent and transition stress may affect the detailed instability processes [e.g., *Houseman and Molnar*, 1997], but their effects were not explored here. However, we think that these rheological parameters mainly affect the results through effective lithospheric viscosity that we investigated extensively in this study.

4.2. Implications for Reactivation Process of the North China Craton

The episodic and multistaged instability of cratonic lithosphere from our studies has implications for the reactivation of the eastern North China Craton with a horizontal length scale of $\sim$1200 km. The magmatism/volcanism associated with the reactivation of the NCC in the Mesozoic and Cenozoic is episodic and the reactivation process may have lasted for $\sim$100 Myr [e.g., *Menzies et al*., 2007], all of which are consistent with the instability process revealed from our study for cratonic lithosphere with non-Newtonian rheology.

That the shallow part of cratonic lithosphere is preferentially destabilized from our non-Newtonian models may have implications for geochemical observations in the NCC. Lithospheric instability has been proposed to explain the presence of crustal eclogitic components in the source for volcanic rocks associated with the reactivation of the NCC [*Gao et al*., 2004, 2008]. Although our models do not include crust, foundering of the shallow part of mantle lithosphere and subsequent emplacement of relatively hot asthenospheric mantle there from our model (Figure 4) may provide the heat source to the lower crust to help form eclogite. Our results show that the shallow part of cratonic lithosphere is significantly heated and weakened by the instability process (Figure 4). This would allow the crustal eclogite to founder into the mantle and then be melted together with the heated cratonic lithosphere, thus explaining the eclogite component in the source of volcanic rocks [*Gao et al*., 2004, 2008]. We think that this geochemical observation may present a challenge to convective entrainment as a mechanism for reactivation of the NCC, because it preferentially erodes the bottom of the lithosphere [e.g., *Beuchert et al*., 2010; *Wang et al*., 2014].

The fate of destabilized cratonic lithospheric materials deserves some discussion, after they sink into the mantle. Some of the materials would be sheared away to other parts of the mantle due to mantle global circulation (not modeled here), but some may be heated, lose its net negative buoyancy and come back to the lithospheric depths [*Fourel et al*., 2013; *Jaupart et al*., 2007] to be mixed with that derived from asthenospheric mantle (Figure 4). This may explain the hybridized magmatic sources of cratonic lithosphere and oceanic mantle found in Cenozoic xenoliths in the NCC [*Zheng et al*., 2001]. Most studies on the NCC

© 2015. American Geophysical Union. All Rights Reserved.

suggest that the cratonic lithosphere was nearly completely removed, based on the seismic and heat flux observations [e.g., *Menzies et al*., 2007; *Zhu et al*., 2012a]. However, our models indicate that a significant fraction of cratonic mantle may remain underneath the NCC, but the instability causes the lithospheric mantle thermally mixed and heated (Figure 4d–f), which may explain the seismic and heat flux observations equally well.

4.3. Lithospheric Viscosity and Cause for the Reactivation of the NCC

The stability of cratonic lithosphere is controlled by lithospheric strength [*Lenardic and Moresi*, 1999; *Shapiro et al*., 1999]. Therefore, the eastern part of the North China Craton must have been weakened significantly before its reactivation [e.g., *Menzies et al*., 2007]. Water released from subduction process may have contributed to the lithospheric weakening [*Hirth and Kohlstedt*, 2003], and this is supported by a recent study that found the high water content in the source of Mesozoic volcanic rocks on the NCC [*Xia et al*., 2013]. Lithospheric yielding associated with subduction may also have contributed to the weakening of overriding plates (i.e., the NCC) [*Lenardic et al*., 2003; *O'Neill et al*., 2009]. Subduction of the Izanagi Plate in the Mesozoic may induce tensional stress that weakens and reactivates the NCC [e.g., *Zhu et al*., 2012a, 2012b]. However, given the long and complicated subduction history around the NCC in the Paleozoic and Mesozoic (Figure 1), it is challenging to establish a cause-effect relation between the subduction process and the initiation of reactivation of the NCC. A number of questions need answers. How is the water delivered to the cratonic lithosphere? Why does subduction of the Izanagi Plate necessarily induce extensional stress in the NCC, considering that other subduction zones produce compressional stress on the overriding plates (e.g., South America)? Does lithospheric yielding remain relevant deformation mechanism at depths of cratonic lithosphere, if the coefficient of friction for lithospheric mantle is >0.25, as suggested by observations of load-induced seismicity and flexure [*Zhong and Watts*, 2013]?

Our current studies, by focusing on lithospheric instability process and its dependence on lithospheric viscosity (or lithospheric Rayleigh number Ra_l), do not directly address the question of lithospheric weakening, hence the cause of reactivation of the NCC. However, as we have demonstrated, it is important to investigate the instability process (i.e., its style and temporal and spatial scales) in order to interpret geological and geochemical observations, even if the cratonic lithosphere is assumed weakened by some processes (e.g., hydration or heightened tectonic stress). The effective lithospheric viscosity is $10^{21}-10^{22}$ Pa s before the instability in our models (Table 2), consistent with that estimated for actively deformed continental lithosphere [*England and Molnar*, 1997; *Flesch et al*., 2000].

A significant simplification in our models is the two-layer viscosity structure (i.e., with η_0 in equation (8)) that only approximates but does not explicitly consider temperature-dependent viscosity, following the simplified viscosity models in *Jaupart et al*. [2007]. Using a temperature-dependent viscosity with an activation energy derived from laboratory studies (e.g., $\sim$400 KJ/mol) would lead to too high cratonic lithospheric viscosity that would prohibit any lithospheric deformation and instability [e.g., *Hirth and Kohlstedt*, 2003]. To examine the effects of temperature-dependent viscosity, we have computed non-Newtonian ($n = 3.5$) models with different activation energy in equation (9). In these calculations, η_w, the prefactor in equation (9), is set to be 30 for cratonic lithosphere (i.e., $C = 1$) to account for melt depletion effect on viscosity [e.g., *Hirth and Kohlstedt*, 2003]. With input Rayleigh number Ra_i ranging from 2×10^7 to 6×10^7 and buoyancy number $B = 0.5$ (i.e., the same as in our reference case NN026), our models suggest that the cratonic lithosphere is largely stable for at least 4.5 Gyr for activation energy greater than 140 KJ/mol. However, with smaller activation energy (e.g., $\sim$100 KJ/mol) that results in a viscosity increase of 3–4 orders of magnitude together with the melt-depletion effect for cratonic lithosphere, the gravitational instability of cratonic lithosphere is similar to that from our simplified two-layer models (Figure 10 for an example case with activation energy of 100 KJ/mol).

While lithospheric viscosity is likely very complicated, we believe that our simplified lithospheric rheology may be partially justified by the field observations. Seismic observations indicate that cold lithospheric mantle can be destabilized and sink into the mantle in different tectonic settings. For example, in the Carpathian-Pannonian region of the central Europe, seismically fast anomalies down to $\sim$400 km depths are interpreted as the destabilized lithosphere that is sufficiently cold to contain abundant seismicity [*Dando et al*., 2011; *Ren et al*., 2012]. In the western US, the foundered lithosphere appears to originate immediately below the Moho [*Levander et al*., 2011; *Molnar and Jones*, 2004]. Particularly, *Molnar and Jones*

©2015. American Geophysical Union. All Rights Reserved.

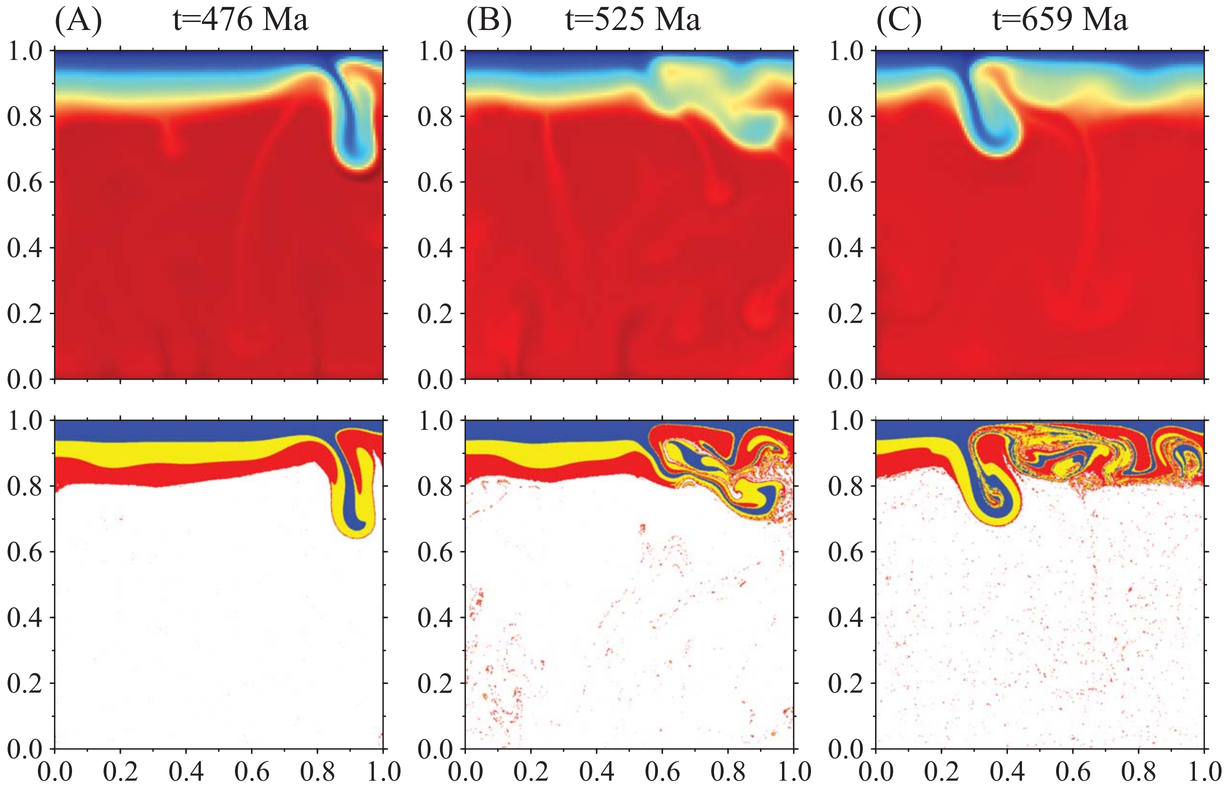

Figure 10. Snapshots of temperature (the upper row) and composition (the lower row) at three different times for a non-Newtonian calculation with temperature-dependent viscosity with activation energy of 100 KJ/mol. Other parameters are $\eta_w = 30$, $Ra_i = 6 \times 10^7$, and B = 0.5. The lithospheric instability is similar to that for non-Newtonian with two-layer viscosity structure, i.e., episodic and multistaged features, and initiation of the instability at the shallower part of the lithosphere.

[2004] estimated that in the Sierra Nevada, tens of kilometers of mantle lithosphere that is colder than 900°C may have been removed through the instability process, suggesting the importance of other lithospheric deformation mechanisms [*Harig et al*., 2010]. Geochemical evidence for crustal eclogite to founder into the mantle [*Gao et al*., 2004, 2008] also suggests that the cold, shallow part of cratonic lithosphere be sufficiently weak during the reactivation. Although the instability mechanism that we present here in this study depends on our simplified two-layer viscosity structure that is clearly different from what has been proposed from laboratory studies in terms of rheological parameters, the model outcomes seem to be supported by these field observations. This highlights the need to bring together field observations, laboratory, and geodynamic modeling studies on lithospheric rheology, as recently stated in *Zhong and Watts* [2013] based on studies on surface loading problems. More future studies are needed to examine how more realistic lithospheric rheology could affect the instability of cratonic lithosphere as investigated in this study.

5. Conclusions

We have formulated 2-D thermochemical convection models to investigate the instability of a compositionally buoyant lithosphere and its temporal and spatial scales. We have computed a large number of simplified two-layer Newtonian and non-Newtonian models with different buoyancy number B and lithospheric Rayleigh number Ra_l. The numerical models show that with non-Newtonian rheology, gravitational instability of a compositionally buoyant layer can happen for buoyancy number B up to 0.7, which is significantly larger than the threshold buoyancy number $B \sim 0.4$ for the instability with Newtonian rheology. Considering that the buoyancy number for cratonic lithosphere is in the range of 0.4–1.0, our results suggest an essential role of non-Newtonian rheology in the instability of cratonic lithosphere.

The instability of cratonic lithosphere (i.e., $B > 0.4$) with non-Newtonian rheology is driven by net negative buoyancy at the shallow depth and tends to destabilize preferentially the shallow part of the lithosphere

© 2015. American Geophysical Union. All Rights Reserved.

with an intrinsically small horizontal length scale ($<\sim$300 km). Such instabilities lead to efficient thermal and chemical mixing of entire cratonic lithosphere, which may explain geochemical mixing inferred for the sources of volcanism/magmatism during the reactivation of the North China Craton. For compositionally buoyant lithosphere with a smaller buoyancy number or Newtonian rheology, the instability destabilizes mantle lithosphere at larger depths with a larger horizontal length scale.

For cratonic lithosphere of horizontal length scale of $\sim$1200 km such as the eastern North Chain Craton, the instability process is episodic and consists of multiple instability events that may last for $\sim$100 Myr to destabilize the entire lithosphere. This is consistent with the observations of episodic magmatism/volcanism events and their $\sim$100 Myr duration in the Mesozoic and Cenozoic for the reactivation of the North China Craton. This consistency, together with efficient thermal and chemical mixing for instability of cratonic lithosphere, suggests that the gravitational instability may play an essential role in the reactivation of the North China Craton.

Acknowledgments
The authors would like to thank Greg Houseman, Peter Molnar, and Editor Thorsten Becker for their insightful and constructive review and comments that significantly improve the paper. This work was supported by NSFC (91014005 and 40774045) to J.H., US-NSF EAR-1135382 and EAR-1015669 to S.Z., and the CAS/SAFEA International Partnership Program for Creative Research Teams. Y.W. and S.Z. also thank 2013 CIDER for providing stimulating discussions on the stability of continental cratons. Data used in this paper can be freely obtained from corresponding author through email request.

References

Afonso, J. C., M. Fernandez, G. Ranalli, W. L. Griffin, and J. A. D. Connolly (2008), Integrated geophysical-petrological modeling of the lithosphere and sublithospheric upper mantle: Methodology and applications, *Geochem. Geophys. Geosyst.*, *9*, Q05008, doi:10.1029/2007GC001834.

Ames, L., G. R. Tilton, and G. Z. Zhou (1993), Timing of collision of the Sino-Korean and Yangtze Cratons—U-Pb zircon dating of coesite-bearing eclogites, *Geology*, *21*, 339–342.

Beuchert, M. J., Y. Y. Podladchikov, N. S. C. Simon, and L. H. Rupke (2010), Modeling of craton stability using a viscoelastic rheology, *J. Geophys. Res.*, *115*, B11413, doi:10.1029/2009JB006482.

Carlson, R. W., D. G. Pearson, and D. E. James (2005), Physical, chemical, and chronological characteristics of continental mantle, *Rev. Geophys.*, *43*, RG1001, doi:10.1029/2004RG000156.

Chen, L., C. Cheng, and Z. G. Wei (2009), Seismic evidence for significant lateral variations in lithospheric thickness beneath the central and western North China Craton, *Earth Planet. Sci. Lett.*, *286*, 171–183.

Conrad, C. P., and P. Molnar (1997), The growth of Rayleigh-Taylor-type instabilities in the lithosphere for various rheological and density structures, *Geophys. J. Int.*, *129*, 95–112.

Conrad, C. P., and P. Molnar (1999), Convective instability of a boundary layer with temperature- and strain-rate-dependent viscosity in terms of 'available buoyancy,' *Geophys. J. Int.*, *139*, 51–68.

Cooper, C. M., A. Lenardic, and L. Moresi (2004), The thermal structure of stable continental lithosphere within a dynamic mantle, *Earth Planet. Sci. Lett.*, *222*, 807–817.

Dando, B. D. E., G. W. Stuart, G. A. Houseman, E. Hegedus, E. Bruckl, and S. Radovanovic (2011), Teleseismic tomography of the mantle in the Carpathian-Pannonian region of central Europe, *Geophys. J. Int.*, *186*, 11–31.

Dixon, J. E., T. H. Dixon, D. R. Bell, and R. Malservisi (2004), Lateral variation in upper mantle viscosity: Role of water, *Earth Planet. Sci. Lett.*, *222*, 451–467.

Duggen, S., K. Hoernle, P. Van den Bogaard, and D. Garbe-Schonberg (2005), Post-collisional transition from subduction- to intraplate-type magmatism in the westernmost Mediterranean: Evidence for continental-edge delamination of subcontinental lithosphere, *J. Petrol.*, *46*, 1155–1201.

Elkins-Tanton, L. T. (2007), Continental magmatism, volatile recycling, and a heterogeneous mantle caused by lithospheric gravitational instabilities, *J. Geophys. Res.*, *112*, B03405, doi:10.1029/2005JB004072.

England, P., and P. Molnar (1997), Active deformation of Asia: From kinematics to dynamics, *Science*, *278*, 647–650.

Flesch, L. M., W. E. Holt, A. J. Haines, and B. M. Shen-Tu (2000), Dynamics of the Pacific-North American plate boundary in the western United States, *Science*, *287*, 834–836.

Foley, S. F. (2008), Rejuvenation and erosion of the cratonic lithosphere, *Nat. Geosci.*, *1*, 503–510.

Fourel, L., L. Milelli, C. Jaupart, and A. Limare (2013), Generation of continental rifts, basins, and swells by lithosphere instabilities, *J. Geophys. Res. Solid Earth*, *118*, 3080–3100, doi:10.1002/jgrb.50218.

Gao, S., R. L. Rudnick, R. W. Carlson, W. F. McDonough, and Y. S. Liu (2002), Re-Os evidence for replacement of ancient mantle lithosphere beneath the North China craton, *Earth Planet. Sci. Lett.*, *198*, 307–322.

Gao, S., R. L. Rudnick, H. L. Yuan, X. M. Liu, Y. S. Liu, W. L. Xu, W. L. Ling, J. Ayers, X. C. Wang, and Q. H. Wang (2004), Recycling lower continental crust in the North China craton, *Nature*, *432*, 892–897.

Gao, S., et al. (2008), Recycling deep cratonic lithosphere and generation of intraplate magmatism in the North China Craton, *Earth Planet. Sci. Lett.*, *270*, 41–53.

Griffin, W. L., Z. Andi, S. Y. O'Reilly, and C. G. Ryan (1998), Phanerozoic evolution of the lithosphere beneath the Sino-Korean Craton, *Geodynamics*, *27*, 107–126.

Griffin, W. L., S. Y. O'Reilly, J. C. Afonso, and G. C. Begg (2009), The composition and evolution of lithospheric mantle: A re-evaluation and its tectonic implications, *J. Petrol.*, *50*, 1185–1204.

Harig, C., S. J. Zhong, and F. J. Simons (2010), Constraints on upper mantle viscosity from the flow-induced pressure gradient across the Australian continental keel, *Geochem. Geophys. Geosyst.*, *11*, Q06004, doi:10.1029/2010GC003038.

Hirth, G., and D. Kohlstedt (2003), Rheology of the upper mantle and the mantle wedge: A view from the experimentalists, in *Inside the Subduction Factory*, edited by J. Eiler, pp. 83–105, AGU, Washington, D. C., doi:10.1029/138GM06.

Houseman, G. A., and P. Molnar (1997), Gravitational (Rayleigh-Taylor) instability of a layer with non-linear viscosity and convective thinning of continental lithosphere, *Geophys. J. Int.*, *128*, 125–150.

Jaupart, C., P. Molnar, and E. Cottrell (2007), Instability of a chemically dense layer heated from below and overlain by a deep less viscous fluid, *J. Fluid Mech.*, *572*, 433–469.

Jordan, T. H. (1978), Composition and development of continental tectosphere, *Nature*, *274*, 544–548.

King, S. D. (2005), Archean cratons and mantle dynamics, *Earth Planet. Sci. Lett.*, *234*, 1–14.

© 2015. American Geophysical Union. All Rights Reserved.

Kusky, T. M., B. F. Windley, and M. G. Zhai (2007), Tectonic evolution of the North China Block: From orogen to craton to orogen, in *Mesozoic Sub-Continental Lithospheric Thinning Under Eastern Asia*, vol. 280, pp. 1–34, Geol. Soc., London.

Lee, C.-T. A., P. Luffi, and E. J. Chin (2011), Building and destroying continental mantle, *Annu. Rev. Earth Planet. Sci.*, *39*, 59–90.

Lenardic, A., and L. N. Moresi (1999), Some thoughts on the stability of cratonic lithosphere: Effects of buoyancy and viscosity, *J. Geophys. Res.*, *104*, 12,747–12,758.

Lenardic, A., L. N. Moresi, and H. Muhlhaus (2003), Longevity and stability of cratonic lithosphere: Insights from numerical simulations of coupled mantle convection and continental tectonics, *J. Geophys. Res.*, *108*(B6), 2303, doi:10.1029/2002JB001859.

Levander, A., B. Schmandt, M. S. Miller, K. Liu, K. E. Karlstrom, R. S. Crow, C. T. A. Lee, and E. D. Humphreys (2011), Continuing Colorado plateau uplift by delamination-style convective lithospheric downwelling, *Nature*, *472*, 461–465.

Li, S. G., et al. (1993), Collision of the North China and Yangtse Blocks and formation of coesite-bearing eclogites: Timing and processes, *Chem. Geol.*, *109*, 89–111.

McNamara, A. K., and S. J. Zhong (2004), Thermochemical structures within a spherical mantle: Superplumes or piles?, *J. Geophys. Res.*, *109*, B07402, doi:10.1029/2003JB002847.

Menzies, M. A., Y. G. Xu, H. F. Zhang, and W. M. Fan (2007), Integration of geology, geophysics and geochemistry: A key to understanding the North China Craton, *Lithos*, *96*, 1–21.

Molnar, P., and C. H. Jones (2004), A test of laboratory based rheological parameters of olivine from an analysis of late Cenozoic convective removal of mantle lithosphere beneath the Sierra Nevada, California, USA, *Geophys. J. Int.*, *156*, 555–564.

Morency, C., and M. P. Doin (2004), Numerical simulations of the mantle lithosphere delamination, *J. Geophys. Res.*, *109*, B03410, doi:10.1029/2003JB002414.

Moresi, L., S. J. Zhong, and M. Gurnis (1996), The accuracy of finite element solutions of Stokes' flow with strongly varying viscosity, *Phys. Earth Planet. Inter.*, *97*, 83–94.

O'Neill, C., A. Lenardic, A. M. Jellinek, and L. Moresi (2009), Influence of supercontinents on deep mantle flow, *Gondwana Res.*, *15*, 276–287.

Podolefsky, N. S., S. J. Zhong, and A. K. McNamara (2004), The anisotropic and rheological structure of the oceanic upper mantle from a simple model of plate shear, *Geophys. J. Int.*, *158*, 287–296.

Pollack, H. N. (1986), Cratonization and thermal evolution of the mantle, *Earth Planet. Sci. Lett.*, *80*, 175–182.

Poudjom Djomani, Y. H., S. Y. O'Reilly, W. L. Griffin, and P. Morgan (2001), The density structure of subcontinental lithosphere through time, *Earth Planet. Sci. Lett.*, *184*, 605–621.

Ren, Y., G. W. Stuart, G. A. Houseman, B. Dando, C. Lonescu, E. Hegedus, S. Radovanovic, Y. Shen, and S. C. P. W. Grp (2012), Upper mantle structures beneath the Carpathian-Pannonian region: Implications for the geodynamics of continental collision, *Earth Planet. Sci. Lett.*, *349*, 139–152.

Schutt, D. L., and C. E. Lesher (2010), Compositional trends among Kaapvaal Craton garnet peridotite xenoliths and their effects on seismic velocity and density, *Earth Planet. Sci. Lett.*, *300*, 367–373.

Seton, M., et al. (2012), Global continental and ocean basin reconstructions since 200 Ma, *Earth Sci. Rev.*, *113*, 212–270.

Shapiro, S. S., B. H. Hager, and T. H. Jordan (1999), Stability and dynamics of the continental tectosphere, *Lithos*, *48*, 115–133.

Sleep, N. H. (2003), Survival of Archean cratonal lithosphere, *J. Geophys. Res.*, *108*(B6), 2302, doi:10.1029/2001JB000169.

Tackley, P. J., and S. D. King (2003), Testing the tracer ratio method for modeling active compositional fields in mantle convection simulations, *Geochem. Geophys. Geosyst.*, *4*(4), 8302, doi:10.1029/2001GC000214.

Wang, H. L., J. van Hunen, D. G. Pearson, and M. B. Allen (2014), Craton stability and longevity: The roles of composition-dependent rheology and buoyancy, *Earth Planet. Sci. Lett.*, *391*, 224–233.

Wang, Y. H., G. A. Houseman, G. Lin, F. Guo, Y. J. Wang, W. M. Fan, and C. X (2005), Mesozoic lithospheric deformation in the North China block: Numerical simulation of evolution from orogenic belt to extensional basin system, *Tectonophysics*, *405*, 47–63.

Wu, F. Y., J. Q. Lin, S. A. Wilde, X. O. Zhang, and J. H. Yang (2005), Nature and significance of the Early Cretaceous giant igneous event in eastern China, *Earth Planet. Sci. Lett.*, *233*, 103–119.

Xia, Q. K., J. Liu, S. C. Liu, I. Kovacs, M. Feng, and L. Dang (2013), High water content in Mesozoic primitive basalts of the North China Craton and implications on the destruction of cratonic mantle lithosphere, *Earth Planet. Sci. Lett.*, *361*, 85–97.

Xiao, W. J., B. F. Windley, J. Hao, and M. G. Zhai (2003), Accretion leading to collision and the Permian Solonker suture, Inner Mongolia, China: Termination of the central Asian orogenic belt, *Tectonics*, *22*(6), 1069, doi:10.1029/2002TC001484.

Xu, Y. G. (2001), Thermo-tectonic destruction of the archaean lithospheric keel beneath the sino-korean craton in china: Evidence, timing and mechanism, *Phys. Chem. Earth Part A*, *26*, 747–757.

Zhang, H. F., M. Sun, X. H. Zhou, M. F. Zhou, W. M. Fan, and J. P. Zheng (2003), Secular evolution of the lithosphere beneath the eastern North China Craton: Evidence from Mesozoic basalts and high-Mg andesites, *Geochim. Cosmochim. Acta*, *67*, 4373–4387.

Zheng, J. P., S. Y. O'Reilly, W. L. Griffin, F. X. Lu, M. Zhang, and N. J. Pearson (2001), Relict refractory mantle beneath the eastern North China block: Significance for lithosphere evolution, *Lithos*, *57*, 43–66.

Zhong, S. J., and A. B. Watts (2013), Lithospheric deformation induced by loading of the Hawaiian Islands and its implications for mantle rheology, *J. Geophys. Res. Solid Earth*, *118*, 6025–6048, doi:10.1002/2013JB010408.

Zhu, R. X., Y. G. Xu, G. Zhu, H. F. Zhang, Q. K. Xia, and T. Y. Zheng (2012a), Destruction of the North China Craton, *Sci. China Earth Sci.*, *55*, 1565–1587.

Zhu, R. X., J. H. Yang, and F. Y. Wu (2012b), Timing of destruction of the North China Craton, *Lithos*, *149*, 51–60.

© 2015. American Geophysical Union. All Rights Reserved.